Supplementary Information for Skyrmionic Spin Structures in Layered Fe$_5$GeTe$_2$ Up To Room Temperature

Maurice Schmitt[1], Thibaud Denneulin[2], András Kovács[2], Tom G. Saunderson[1,3], Philipp Rüßmann[4, 3], Aga Shahee[1], Tanja Scholz[5], Amir Tavabi[2], Martin Gradhand[1,6], Phivos Mavropoulos[7], Bettina V. Lotsch[5, 8], Rafal Dunin-Borkowski[2], Yuriy Mokrousov[3], Stefan Blügel[3], and Mathias Kläui*[1, 9]

[1]Johannes Gutenberg Universität Mainz, Institut für Physik, Staudingerweg 7, 55128 Mainz, Germany
[2]Ernst Ruska-Centre for Microscopy and Spectroscopy with Electrons and Peter Grünberg Institute, Forschungszentrum Jülich, 52425 Jülich, Germany
[3]Peter Grünberg Institut and Institute for Advanced Simulation, Forschungszentrum Jülich, 52425 Jülich, Germany
[4]Institute of Theoretical Physics and Astrophysics, University of Würzburg, Am Hubland, 97074 Würzburg, Germany
[5]Max Planck Institute for Solid State Research, Heisenbergstraße 1, 70569 Stuttgart, Germany
[6]University of Bristol, School of Physics, HH Wills Physics Laboratory, Tyndall Avenue, Bristol BS8 1TL, England
[7]National and Kapodistrian University of Athens, Department of Physics, University Campus, GR-157 84 Zografou, Athens, Greece
[8]Department of Chemistry, University of Munich (LMU), Butenandtstraße 5-13 (Haus D), 81377 München, Germany
[9]QuSpin, Norwegian University of Science and Technology, Department of Physics, NTNU NO-7491, Trondheim, Norway

klaeui@uni-mainz.de

Supplementary Note 1: Magnetic anisotropy in Fe$_5$GeTe$_2$

Isothermal magnetization vs. magnetic field (M vs. H) curves measured using a SQUID, under the applied field either parallel to the c-axis ($B_{\text{c-axis}}$) or the ab plane ($B_{\text{ab-plane}}$) are shown in Fig. 4 of the main text. Fig. 4(a) and (b) are for the pre-cooling phase and Fig. 4(c) and (d) for the post-cooling phase respectively. These magnetization curves are presented without taking into consideration the demagnetization factor, which plays a great role in defining the internal field in 2D flake-like and 1D needle-like crystals. These M vs. H curves indicate a soft ferromagnetic nature of both the pre-cooling and post-cooling phases with a weak magneto-crystalline anisotropy. The raw data indicates a smaller external field is needed to saturate magnetization in the ab-plane than along the c-axis, which may at first indicate that Fe$_5$GeTe$_2$ is an easy plane ferromagnet. However, consideration of the large contribution to internal field from the demagnetization factor for the c-axis configuration indicates an opposite behavior, where spins prefer to align along the c-axis, as has been reported by May et al. [1]. The samples used in this paper are explicitly confirmed to be out-of-plane easy axis systems by direct L-TEM imaging, which is not affected by demagnetization factor considerations and thus more robust. The results are shown in the following.
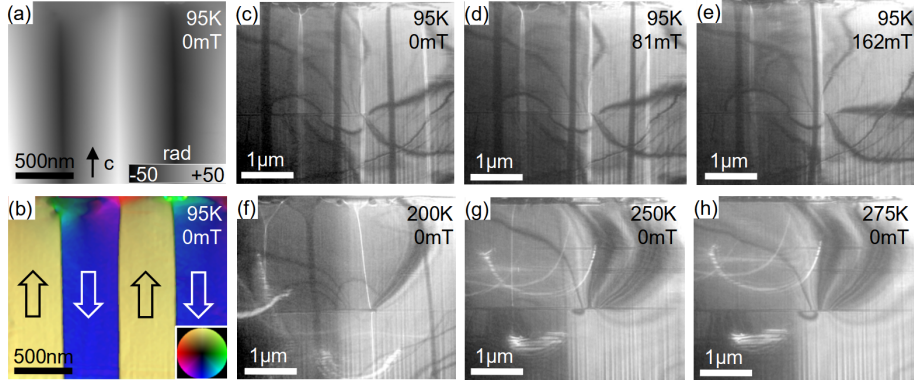

Fig. S1: **L-TEM images of a Fe$_5$GeTe$_2$ lamella with the crystallographic c-axis in the image plane.** (a) phase shift image obtained using off-axis electron holography at 95 K and 0 mT in a cross-section lamella (c-axis is vertical in the image plane). (b) Corresponding color-coded magnetic induction map where the direction of the magnetic field is given by the color wheel in the bottom right corner. (c-e) Fresnel images obtained at 95 K and different external fields indicated on the images and with a defocus of -1 mm. (f-h) Fresnel images obtained at 0 mT and different temperatures indicated on the images.

Further, we investigated magnetic domains in lamellas cut from Fe$_5$GeTe$_2$ crystals parallel to the c-axis. Fig. S1(a,b) shows a phase shift image and the corresponding color-coded magnetic induction map obtained at 95 K and 0 mT. The presence of 180° stripe domains with domain walls (DWs) orientated along

the [001] direction confirm the easy axis magnetic anisotropy of Fe_5GeTe_2 with the c-axis (001) as the easy axis. Fig. S1(c-h) shows Fresnel defocus images obtained in the presence of different external fields applied nearly perpendicular to the c-axis (0 to 162 mT) and at different temperatures (95 to 275 K). Even though the domain walls move in the presence of external fields and the width of the domains changes as a function of temperature, it can be observed that the DWs remain parallel to the c-axis even close to T_C at 250 K for instance, which confirms the easy axis magnetic anisotropy of Fe_5GeTe_2 over a wide range of temperatures, which as shown in the main text, we have observed directly using L-TEM.

Supplementary Note 2: Determination of the saturation magnetization from the stripe domain pattern

An independent way to determine the saturation magnetization is to closely examine the stripe domain patterns seen in the L-TEM images. This way, the validity of the SQUID results can be checked. According to theoretical considerations [2], the saturation magnetization of a film of magnetic material is given by

$$M_s = 2 \cdot \frac{a^2}{t} \cdot \frac{(B_c - B)/\mu_0}{\pi r_{\downarrow c}} \, , \tag{S1}$$

where μ_0 is the magnetic vacuum permeability, M_s is the saturation magnetization, a is the overall domain periodicity, t is the film thickness, $r_{\downarrow c}$ is the width of the minority spin domains, and B and B_c are an arbitrarily chosen field and the saturating field, respectively. This theory assumes the considered sample is a magnetic film with uniaxial anisotropy and a large domain period, and considers exchange, Zeeman, anisotropy, and stray field energy contributions. The film thickness in our sample is not uniform, as scanning electron microscopy (SEM) measurements on various spots of the sample reveal. However, the measured local thicknesses all range from 90 nm to 210 nm, so the film thickness can be estimated to be $t = (150 \pm 60)$ nm. All other parameters on the right hand side of equation S1 can be estimated from the recorded TEM images. The domain periodicity a at the chosen field $B = 0$ mT can be estimated by adding the length of both blue lines in Fig. S2 and dividing by eight, since both blue lines together span a total of eight domain periods. The average length of the red lines is used to estimate $r_{\downarrow c}$. Since no magnetic contrast is visible at 655 mT anymore, the saturating field is estimated to be $B_c = (550 \pm 100)$ mT in this case. This method leads to a relatively large uncertainty in the minority domain width, since it is not only a relatively small distance to measure, but also because the measured widths cannot be measured exactly at the critical field. Therefore, each individual red line can be estimated to have an error of 50 %, which propagates to yield the average length of all lines of $r_{\downarrow c} = (53.6 \pm 10.2)$ nm. Via the same method, the domain periodicity is estimated to be $a = (272.1 \pm 96.5)$ nm.

Accordingly, using error propagation, the obtained saturation magnetization is $M_s = (2.56 \pm 1.52) \cdot 10^6$ A m^{-1}. Although this way the saturation magnetization has a larger relative uncertainty, its order of magnitude agrees with the
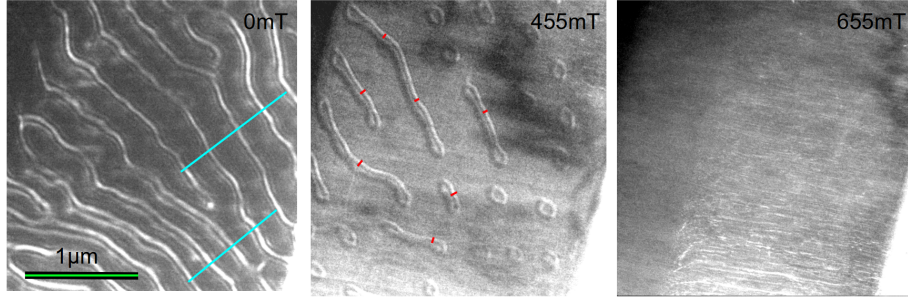
Fig. S2: **L-TEM images of Fe$_5$GeTe$_2$ at 95 K.** The red lines are used to estimate the minority stripe domain width, whereas the blue lines are used to determine the overall domain periodicity. The green line is used to convert lengths in pixels to real lengths. The c-axis is perpendicular to the image plane.

values obtained from the SQUID measurements, thus confirming the validity of the SQUID measurements.

Supplementary Note 3: Determination of the micromagnetic exchange constant from the Curie temperature

To confirm the results obtained from DFT, the micromagnetic exchange constant (or spin stiffness) will be approximated in the following. To this end, one can invoke a simple Heisenberg model, in which the complex material Fe$_5$GeTe$_2$ is approximated as an isotropic material with one atom per unit cell and nearest neighbor interactions only. This model predicts in a mean-field approach [3]:

$$ J_{\mathrm{H}} = \frac{3kT_{\mathrm{C}}}{2\epsilon z} \tag{S2} $$

where k is the Boltzmann constant, T_{C} is the Curie temperature, z is the number of nearest neighbors in a unit cell and J_{H} is the Heisenberg exchange constant between magnetic sites. The parameter ϵ is a correction factor accounting for spin waves, which is slightly smaller than one and is well-known for common crystal structures [4]. Here, we will simply estimate $\epsilon = 0.8 \pm 0.1$. One can then find the micromagnetic exchange constant $A_{\mathrm{H}}^{\mathrm{IP}}$ according to equation (7) in the main text, by assuming $J_{ij} = J_H$ for nearest neighbors only and averaging the sum over nearest neighbors as well as the nearest neighbor distance squared r_{ij}^2:

$$ A_{\mathrm{H}}^{\mathrm{IP}} = J_H \cdot \frac{z \cdot \overline{r_{ij}^2}}{2V} \ , \tag{S3} $$

with the volume per iron atom V and the average squared neighbor distance $\overline{r_{ij}^2}$. Combining S2 and S3 yields

$$ A_{\mathrm{H}}^{\mathrm{IP}} = \frac{3kT_{\mathrm{C}}}{4\epsilon} \cdot \frac{\overline{r_{ij}^2}}{V} \ , \tag{S4} $$

The Curie temperature $T_C = (310 \pm 10)\,\text{K}$ can be estimated from the SQUID data. Note that in Fe_5GeTe_2 the Curie temperature changes depending on the thermal phase it is in. The larger value of $T_C = (310 \pm 10)\,\text{K}$ is valid for the post-cooling phase. The volume per magnetic site is $V = 0.0276\,\text{nm}^3$ according to the DFT results. For the mean squared neighbor distance, all neighbors in table S1 are considered and averaged over. Here, the split site nature of the Fe_1 site has to be considered, by weighting them only 50%. The result is $\overline{r_{ij}^2} \approx 0.06594\,\text{nm}^2$. Inserting these values into equation S4 yields

$$A_H^{IP} = (0.060 \pm 0.007)\,\text{eV nm}^{-1} . \tag{S5}$$

The value of the micromagnetic exchange constant obtained this way A_H is close to the value obtained via DFT A_{DFT}. Considering that many assumptions are made when calculating the micromagnetic exchange constant via the critical temperature due to the complex crystal structure of Fe_5GeTe_2, the obtained value A_H turns out to be compatible with the more robust DFT result A_{DFT} and thus supports it.

type	Neighbor	Number of neighbors	Bond length
Fe_1	Fe_3	3	2.35 Å
Fe_1	Fe_2	3	2.74 Å
Fe_2	Fe_3	3	2.59 Å
Fe_2	Fe_3	1	2.54 Å
Fe_2	Fe_1	3	2.74 Å
Fe_3	Fe_2	1	2.54 Å
Fe_3	Fe_2	3	2.59 Å
Fe_3	Fe_1	3	2.35 Å

Table S1: The distances between individual iron sites in Fe_5GeTe_2 assuming the space group $R\bar{3}m$.

Supplementary Note 4: Determination of T_C using the J_{ij} elements from DFT

In order to further confirm the validity of our DFT models and calculations, the critical temperature of Fe_5GeTe_2 has been determined by using both the mean-field approximation for multiple atoms in the unit cell [5, 6] and a Monte Carlo [7] method.

In the mean-field approximation we calculate two separate values for the Curie temperature. The first is an effective 2-dimensional Curie temperature, T_C^{2D}, which we obtain by considering purely the intra-layer J_{ij} terms (i.e., we neglect the interactions between atoms over the van-der-Waals gap), which yields $T_C^{2D} = 551\,\text{K}$. The second is a bulk Curie temperature, T_C^{3D}, which additionally contains the inter-layer J_{ij} terms, yielding $T_C^{3D} = 871\,\text{K}$. This shows that the inter-layer interactions have a significant contribution.

The mean-field approximation is known to overestimate the Curie temperature of the Heisenberg model. The Monte-Carlo method much better approximates the exact result. Our calculation, including a $24 \times 24 \times 10$ supercell (28800 atoms including disorder) yields a susceptibility peak at $T_C^{MC} = 380\,\text{K}$.

The T_C determined from the Monte Carlo method is within 25% difference relative to the experimental T_C. As the independent determination of T_C through the J_{ij} terms is comparable to the experiment, it further justifies their use to determine K_δ in equations (11) and (12) in the main text.

Supplementary Note 5: Domain wall widths using the J_{ij} terms from DFT

To further analyse the determination of the exchange parameter A^{DFT}, we turn to atomistic simulations using the *Spirit* code to use the J_{ij} terms to accurately determine a domain wall width. By simulating a domain wall we can further justify our use of A^{DFT} in the determination of the experimental value of K^δ. Firstly, we additionally determine K^{DFT} directly from the juKKR package giving a value of $K^{\mathrm{DFT}} = 24 \cdot 10^{-3} \, \mathrm{eV} \, \mathrm{nm}^{-3}$. This value is approximately a factor of 30 too large compared to experiment, however this quantity is determined from the bulk when in reality the domain wall is on the surface. This quantity can therefore be considered unknown and hence free to be determined. For our simulations we chose a $100 \times 20 \times 10$ supercell consisting of 200,000 spins in the simulation where periodic boundary conditions are chosen in $\vec{b}$ and $\vec{c}$ directions whereas open boundary conditions are used in the $\vec{a}$ direction. The first and last plane of spins in the $\vec{a}$ direction are then fixed in opposite ($\pm z$) directions which enforces a domain wall to form in the center of the simulation box. We solve the Landau-Lifshitz-Gilbert equation with the *Spirit* code [8] where the Depondt solver is applied for a maximum of 100,000 time steps with a maximal simulation time of $1,000 \, \mathrm{ps}$ to relax the magnetic texture. These simulations include the effect of temperature noise which is varied between 0 and 300 K. Fig. S3(a) is a plot of the domain wall width at 95 K for different choices of K^{DFT} within the range of experimental values of K. For large K t domain wall is shortened significantly compared to the experimental values and is hence not necessary to go beyond 0.7 meV/Fe. As the anisotropy constant decreases we see a rather flat distribution until 0.2 meV/Fe at which point the domain wall diverges for vanishing K. Choosing a particular value for $K = 0.04 \, \mathrm{meV/Fe}$ to match with the experimental value, Fig. S3(b) shows how the domain wall evolves as a function of temperature. We observe a steadily increasing value for the domain wall width with temperature, crossing $\delta = 23.2 \, \mathrm{nm}$ at 100K and $\delta = 27.7 \, \mathrm{nm}$ at 200K. This is in good agreement with experimentally determined domain walls when using the experimental anisotropy instead of the value determined by DFT which is more specific to the bulk. Three exemplary domain wall fit at temperatures of 20 K, 100 K and 300 K are shown in Fig. S4(a-c).

Supplementary Note 6: Discussion of the stabilization mechanism of the observed skyrmionic bubbles

There are mainly four stabilization mechanisms typically considered for skyrmions and skyrmionic bubbles: frustrated exchange interactions [9], four-spin interactions, dipolar interactions [10] and DMI [11]. While the dipolar interactions
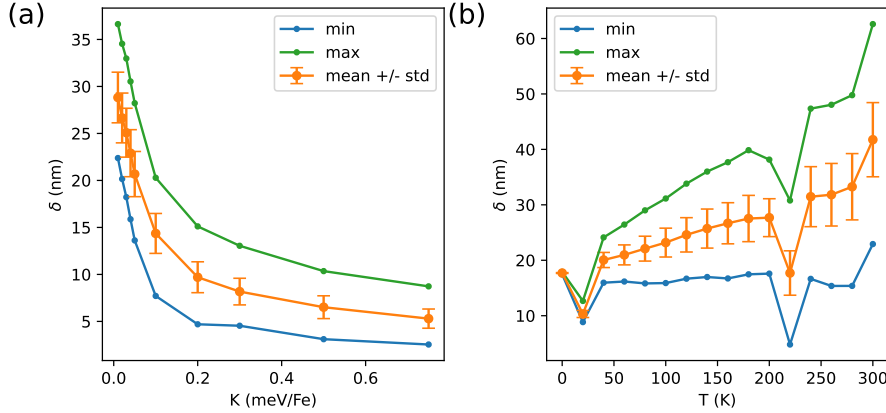
Fig. S3: **Domain Wall widths using *ab initio* J_{ij}'s as a function of anisotropy and temperature**. (a) The domain wall width at $95\,\text{K}$ as a function of anisotropy constant K. (b) The domain wall width with increasing temperature in the simulation. Green and blue lines are indicate the maximal and minimal determined values from the different lines of the Fe atom positions in the unit cell and among the multiple unit cell in the $200 \times 20 \times 10$ cell large supercell. The orange line gives the average over the 20×10 unit cell cross section parallel to the domain wall. The error bars represent the standard deviation (std).

and DMI are the most prevalent stabilization mechanisms [12], frustrated exchange and four-spin interactions can generally not be excluded as potential stabilization mechanisms without further analysis. In this section, the stabilization mechanisms of the bubbles observed in the present work are discussed based on DFT calculations.

Fig. S5 shows the exchange parameters J_{ij} and DMI parameters D_{ij} obtained from DFT calculations of Fe_5GeTe_2 as a function of the distance between spin sites. Firstly, DMI is observed to generally be weak. This is in line with the achirality of the skyrmionic bubbles observed with the L-TEM in the main text. Furthermore, the shown, dominant values of J_{ij} are positive. Consequently, it is unlikely that Fe_5GeTe_2 is a significantly frustrated magnet, which means that frustrated exchange interactions are unlikely to be the stabilization mechanism of the bubbles we observe.

Four-spin interactions are generally a rare source of stabilization. While we do not have any data to exclude four-spin interactions as possible stabilization mechanisms, we deem them unlikely to be the source of stabilization in Fe_5GeTe_2 due to their general rarity and no previous reports of these in related compounds.

Finally, dipolar interactions remain as the only likely source of stabilization of the observed skyrmionic bubbles. While all other stabilizing mechanisms have been argued to likely be negligible, dipolar interactions are relatively strong considering that the observed bubbles are relatively large and reach maximum radii of over $100\,\text{nm}$.
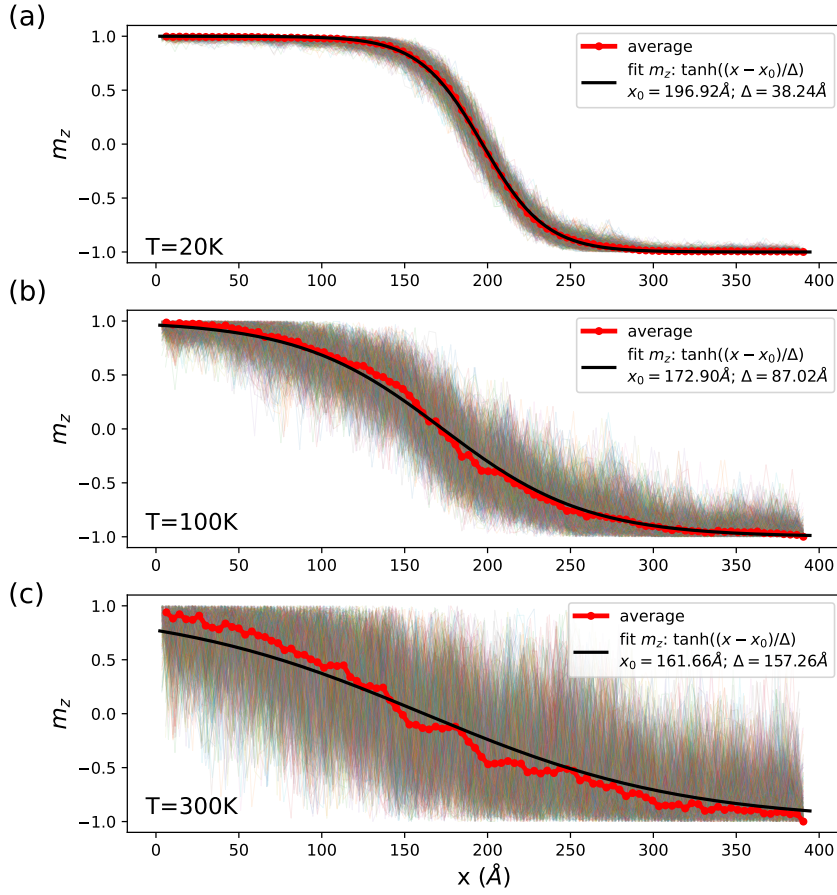
Fig. S4: **Simulated domain Wall profiles**. (a-c) Profiles of the domain wall across all lines of Fe atoms in the 20×10 cell cross section of the Spirit supercell for increasing temperature of 20 K, 100 K and 300 K. The faint lines in the background are the inividual line profiles where the temperature fluctuations are visible. The thick red lines show the average over the lines and the black line the fitted domain wall profile. The simulation uses the *ab initio* J_{ij}'s and the optimized value of the anisotropy of $K = 0.04 \, \text{eV/Fe}$. For large temperatures the fit starts to deviate from the average line (most visible in c) which is attributed to finite size effects in the simulation.

Supplementary Note 7: Field dependent L-TEM images in the pre-cooling and post-cooling phase at $95 \, \text{K}$

The field-dependence of the magnetic structures in Fe_5GeTe_2 at $95 \, \text{K}$ in both thermal phases are shown in Fig. S6. The images have been recorded using the same field sweep method as in the main text. Bubbles occur at all fields at 95K in the pre-cooling phase, as already seen in Fig. 2d in the main text. However,
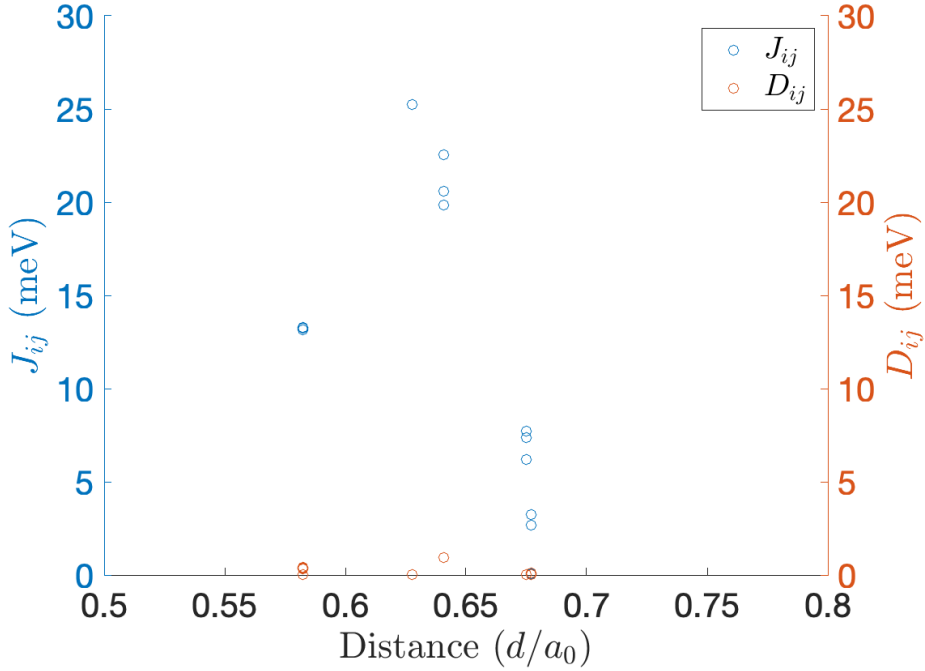
8

Fig. S5: **DFT exchange parameters J_{ij} and DMI parameters D_{ij} as a function of distance between spin sites.** The distances on the horizontal axis have been normalized to the in-plane lattice constant a_0.

in the post-cooling phase, bubbles only occur slightly below the saturation field. These bubbles are accordingly small. The fact that bubbles are more easily stabilized in the pre-cooling phase suggests that Fe_5GeTe_2 might exhibit a larger magnetization in the post-cooling phase.

Supplementary Note 8: Structural aspect of the irreversible phase transition of Fe_5GeTe_2

In order to indicate the structural change that occurs in the irreversible magnetostructural phase transition around $100\,K$ in Fe_5GeTe_2, we have carried out X-ray diffraction (XRD) measurements along the c-axis at room temperature in both phases. The results are shown in Fig. S7. As one can see, there is a significant shift of the peaks corresponding to the pre-cooling phase when compared to the peaks corresponding to the post-cooling phase. These consistent shifts from larger angles in the pre-cooling phase to smaller angles in the post-cooling phase show that the van der Waals stacking has been affected while Fe_5GeTe_2 underwent the phase transition. Explicitly, the c-axis has expanded when the material entered the post-cooling phase. Furthermore, the widths of the peaks are decreased after the phase transition, which suggests that strain has been relaxed in the material. These observations are in line with previous studies [1].

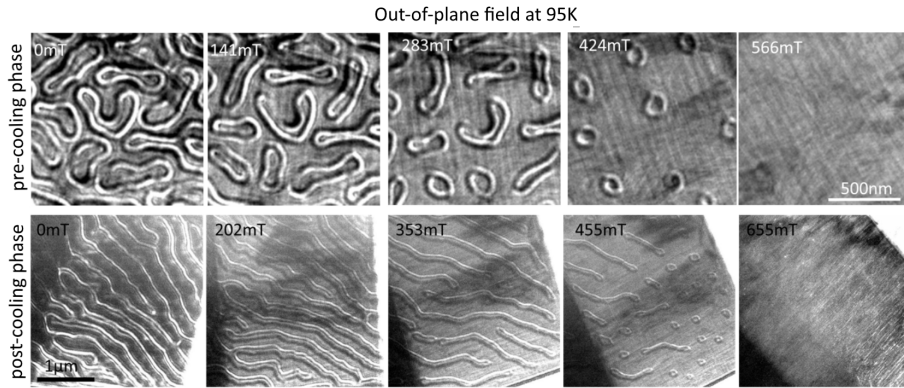To further examine this point, L-TEM electron diffraction patterns are

Fig. S6: **Direct comparison of the field dependence of the magnetic structures in Fe$_5$GeTe$_2$ at $95\,\mathrm{K}$ in the pre-cooling and post-cooling phases.** Bubbles occur at all applied fields in the pre-cooling phase. Stripe domains occur at low to moderate fields in the post-cooling phase and small bubbles only occur slightly below the saturation field. The images are plan-view Fresnel images. The pre-cooling images have been recorded using a defocus of $600\,\mu\mathrm{m}$ and a tilt of $5°$, while the post-cooling images have been recorded using a defocus of $1000\,\mu\mathrm{m}$ and a tilt of $3°$.

recorded both in the pre-cooling and post-cooling phases on the same sample. The results are shown in Fig. S8. In pre-cooling phase, only a few stacking faults located near the surface of the sample are observed. In the post-cooling phase, a large density of stacking faults is observed everywhere on the sample. The diffraction pattern shows additional streaks along the c-axis due to the stacking faults.
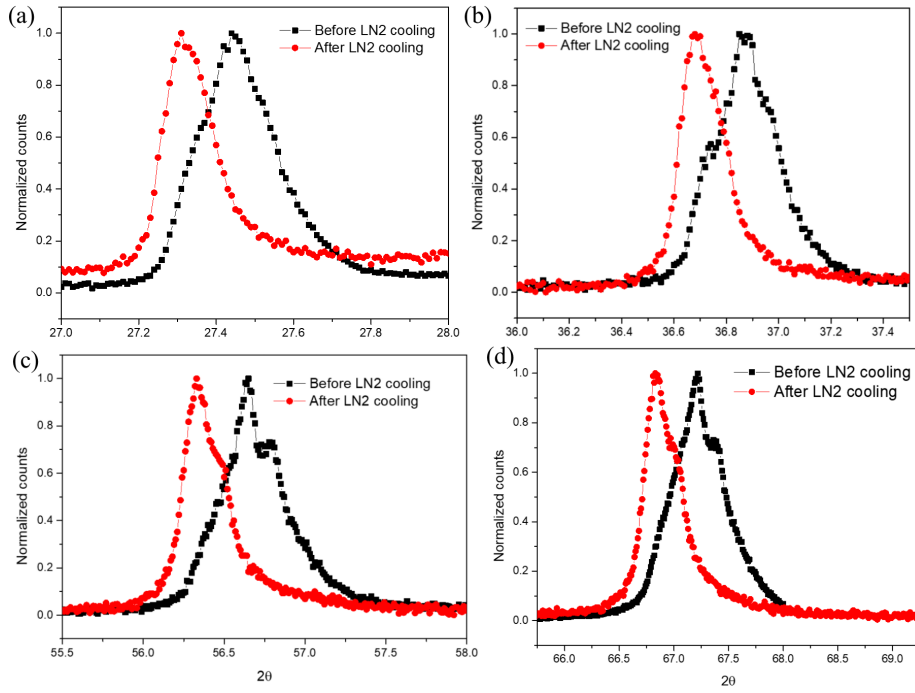
Fig. S7: **XRD measurements showing that the c-axis has been significantly affected by the irreversible phase transition of Fe_5GeTe_2.** Each XRD peak is shifted to slightly lower angles when Fe_5GeTe_2 undergoes the phase transition from the pre-cooling to the post-cooling phase. The panels show the $00l$ XRD peaks, where (a) $l = 9$, (b) $l = 12$, (c) $l = 18$ and (d) $l = 21$ according to space group $R\bar{3}m$
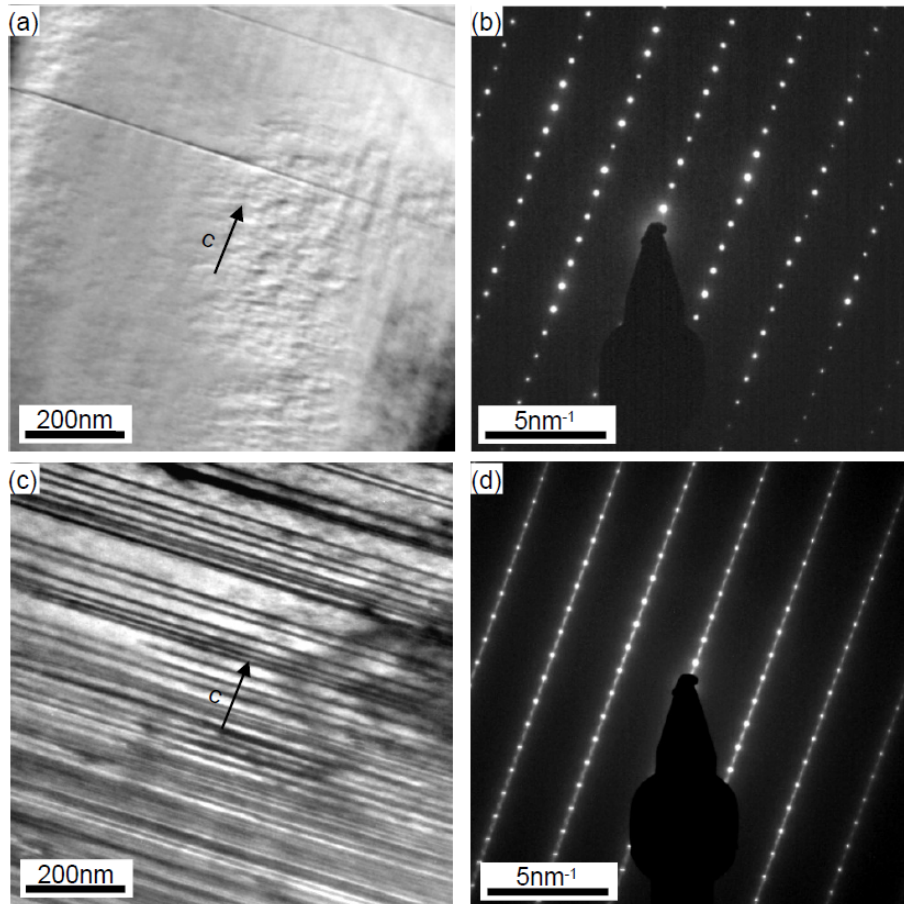
Fig. S8: **Electron diffraction pattern to compare the density of stacking faults in the pre-cooling and post-cooling phase.** (a) Bright-field TEM image and (b) diffraction pattern of Fe_5GeTe_2 in the pre-cooling phase obtained at room temperature with the c-axis oriented in the image plane. (c) Bright-field TEM image and (d) diffraction pattern of the post-cooling phase obtained at room temperature after leaving the sample in liquid nitrogen for one hour. The diffraction patterns (b, d) are aligned such that the reciprocal c^*-axis is parallel to the c-axis depicted in (a, c).

Supplementary References

1. May, A. F. *et al.* Ferromagnetism Near Room Temperature in the Cleavable van der Waals Crystal Fe5GeTe2. *ACS Nano* **13,** 4436–4442 (2019).

2. Johansen, T. H., Pan, A. V. & Galperin, Y. M. Exact asymptotic behavior of magnetic stripe domain arrays. *Phys. Rev. B* **87,** 060402 (2013).

3. Evans, R. F. L. *et al.* Atomistic spin model simulations of magnetic nanomaterials. *J. Phys. Condens. Matter* **26,** 103202 (2014).

4. Garanin, D. A. Self-consistent Gaussian approximation for classical spin systems: Thermodynamics. *Phys. Rev. B* **53,** 11593–11605 (1996).

5. Şaşıoğlu, E., Sandratskii, L. M., Bruno, P. & Galanakis, I. Exchange interactions and temperature dependence of magnetization in half-metallic Heusler alloys. *Phys. Rev. B* **72,** 184415 (2005).

6. Anderson, P. W. Theory of Magnetic Exchange Interactions:Exchange in Insulators and Semiconductors. *J. Phys. C. Solid State Phys.* **14,** 99–214 (1963).

7. Landau, D. & Binder, K. A guide to Monte-Carlo Simulations in Statistical Physics, Cambridge University Press. *Cambridge University Press* (2000).

8. Müller, G. P. *et al.* Spirit: Multifunctional framework for atomistic spin simulations. *Phys. Rev. B* **99,** 224414 (2019).

9. Okubo, T., Chung, S. & Kawamura, H. Multiple-q States and the Skyrmion Lattice of the Triangular-Lattice Heisenberg Antiferromagnet under Magnetic Fields. *Phys. Rev. Lett.* **108,** 017206 (2012).

10. Garel, T. & Doniach, S. Phase transitions with spontaneous modulation-the dipolar Ising ferromagnet. *Phys. Rev. B* **26,** 325–329 (1982).

11. Nagaosa, N. & Tokura, Y. Topological properties and dynamics of magnetic skyrmions. *Nat. Nanotechnol.* **8,** 899–911 (2013).

12. Göbel, B., Mertig, I. & Tretiakov, O. A. Beyond skyrmions: Review and perspectives of alternative magnetic quasiparticles. *Phys. Rep.* **895,** 1–28 (2021).